Water **2014**, *6*, 642-660; doi:10.3390/w6030642

OPEN ACCESS

water

ISSN 2073-4441

www.mdpi.com/journal/water

Article

Improving Sediment Transport Prediction by Assimilating Satellite Images in a Tidal Bay Model of Hong Kong

Peng Zhang [1,2], Onyx W.H. Wai [2], Xiaoling Chen [1], Jianzhong Lu [1,*] and Liqiao Tian [1]

[1] State Key Laboratory of Information Engineering in Surveying, Mapping and Remote Sensing, Wuhan University, Wuhan 430079, China; E-Mails: peterwin86@gmail.com (P.Z.); cecxl@yahoo.com (X.C.); tianye2003@gmail.com (L.T.)

[2] Department of Civil and Environmental Engineering, The Hong Kong Polytechnic University, Kowloon, Hong Kong, China; E-Mail: onyx.wai@polyu.edu.hk (O.W.H.W.)

* Author to whom correspondence should be addressed; E-Mail: lujzhong@163.com; Tel.: +86-27-6877-8755.

Received: 7 January 2014; in revised form: 13 March 2014 / Accepted: 17 March 2014 / Published: 24 March 2014

Abstract: Numerical models being one of the major tools for sediment dynamic studies in complex coastal waters are now benefitting from remote sensing images that are easily available for model inputs. The present study explored various methods of integrating remote sensing ocean color data into a numerical model to improve sediment transport prediction in a tide-dominated bay in Hong Kong, Deep Bay. Two sea surface sediment datasets delineated from satellite images from the Moderate Resolution Imaging Spectra-radiometer (MODIS) were assimilated into a coastal ocean model of the bay for one tidal cycle. It was found that remote sensing sediment information enhanced the sediment transport model ability by validating the model results with *in situ* measurements. Model results showed that root mean square errors of forecast sediment both at the surface layer and the vertical layers from the model with satellite sediment assimilation are reduced by at least 36% over the model without assimilation.

Keywords: sediment transport model; satellite image; optimal interpolation; data assimilation; MODIS; Deep Bay

---

1. Introduction

Suspended sediment particles are an integral part of ecosystem health in many coastal environments, because it is related to the total production and fluxes of heavy metals and micro-pollutants. The knowledge of the suspended sediment transport is critical to water quality management in the coastal ocean area [1]. Numerical models have long been the primary tools employed for understanding and assessing sediment movement in coastal and ocean environmental systems, in particular recent state-of-the-art fine-resolution models have led to fruitful outcomes in these research areas. However, predicting the transport and fate of coastal sediment is still a challenge, because of the highly complex nonlinear sediment dynamics and the lack of understanding of the key sediment processes underlying the behavior of a real-world dynamical system [2]. The state-of-the-art regional-scale sediment transport models, which are based on semi-empirical relationships, would suffer from significant uncertainty of the predictions, unless constrained with observations [3]. Traditionally, observations used for model initialization, calibration and validation have been collected by ship-based surveys or fixed moorings. Such methods usually acquire data with sparse spatial and temporal density and could be very costly.

Satellite ocean color data can provide sea surface sediment information that is highly resolved in both space and time. This is a promising source of data that matches very well to the models' spatial scales and has been proven to be valuable for model evaluation and development [4,5]. However, satellite observations generally have long temporal frequencies and are limited to the surface. On the contrary, numerical models could have no time or space limitations. Numerical models can potentially provide the missing information of the causes of distributions and changes seen in two successive remote sensing observations, as numerical models are built on fundamental principles of ocean physics [6]. Therefore, combining both the advantages of remote sensing data and numerical models can enhance our knowledge on sediment movement. In fact, integrating remote sensing data and numerical simulation has been widely applied in studying ocean and inland water environments. Pleskachevsky *et al.* [7] presented a three-dimensional SPM transport model in synergy with a two-dimensional suspended sediment distribution from ocean color (CZCS) images to analysis the resuspension and deposition characteristic of vertical sediment. Miller *et al.* [8] used sediment concentration derived from cloud-free Moderate Resolution Imaging Spectra-radiometer (MODIS) images to calibrate and validate the output of the sediment transport model by comparing with the model predicted SPM concentrations. Kouts *et al.* [9] analyzed the effect of sand dredging on the sediment dynamics of Pakri Bay, Finland, by comparing distributions from remote sensing images and numerical model results. Chen *et al.* [10] proposed an application using a sediment concentration distribution from MERIS images to initialize and calibrate a three-dimensional sediment transport model of Bohai Bay, China.

However, apart from the numerical uncertainties existing in numerical models, satellite data may also suffer from problems coming from on-board acquisition and image interpretation methods [4]. Integrating a model with satellite images without considering their errors may aggravate the uncertainties in the model prediction. The accuracy of model results could be improved through data assimilation, by which models can be regulated in a way that the system's dynamics is strongly complied with and errors in both models and satellite observations are acknowledged. Many

researchers have shown interests in studying remote sensing sediment assimilation in coastal and ocean models. Yet, the corresponding literature is scarce; but the number of publications is growing [4,11–13].

In the present study, a three-dimensional hydrodynamic and sediment transport model of Deep Bay, a tide-dominated bay in Hong Kong, has been established and used to assimilate sea surface sediment data derived from MODIS images. Deep Bay suffers from many environmental problems related to suspended sediment, including high turbidity and seriously contaminated wetland by heavy metals and nutrient sediment pollution, because of the high intensity of human activities [14]. The purpose of this work is to explore the combination of a sediment transport model and satellite images through data assimilation schemes to improve the understanding of the complicated sediment dynamics of Deep Bay. Such an investigation is important to enable better water quality management and wetland ecology restoration of the Bay.

The remainder of this paper is organized as follows. Section 2 introduces the case study region and observational datasets and outlines the hydrodynamic and sediment transport models. Section 3 describes the satellite data processing method and the data assimilation scheme, which integrates the sediment transport model with the remote sensing data. Section 4 presents the model calibration and validation processes and discusses the data assimilation results. Conclusions are given in the last section.

2. Materials and the Model

2.1. Study Area and In Situ Data

Deep Bay (22.41° to 22.53° N, 113.88° to 114.00° E) is a semi-enclosed shallow bay on the eastern side of the Pearl Estuary, between Shenzhen to the north and the New Territories of Hong Kong to the south (Figure 1A). The width of the bay varies from 4 km to 7.6 km at the narrowest section near the mouth. The length is 13.9 km, and the total sea surface area is about 80 km^2. It is influenced by the irregular mixed semi-diurnal tide of the South China Sea. Four major rivers (Shenzhen, Dasha, Yuen Long and Tin Shui Wai River) discharge into the bay with relatively small flow rates. Because of its unique geographic location, the embayment exhibits complicated tidal and sediment movement, subjected to tidal flushing and river outflows, as well as human activities, like reclamation [15]. Deep Bay is important for the conservation of the Futian National Nature Reserve (FNNR) and the Mai Po Nature Reserve (MPNR). These wetlands are located near the mouth of Shenzhen River at the upstream of Deep Bay and provide a habitat for numerous rare and endangered species [16]. The wetlands have been suffering from increasing contamination problems in the region, for example, the adsorption and release of heavy metals and organic pollutants from sediments in the water and sea bottom [17].

Measurements used in this study are parts of the synchronous survey project in the Shenzhen River Basin, which were conducted by the Hydrology Bureau of the Yangtze River Water Resources Commission of China. The project was commenced in October, 2004, during which the measurements were taken hourly from 11:00, on 17 October, to 15:00, on 18 October (in total, 29 h). Water levels were taken by means of tidal gauges placed at Dong Jiao Tou (DJT), Tsim Bui Tsui (TBT), Chi Wan and Lan Kok Tsui (See Figure 1). The vertical profiles of flow velocity, sediment concentration and salinity data were collected at sites located along three transects inside the bay. Transect A is to the

northwest of Deep Bay near the mouth of the Shenzhen River. There are three observation sites: S4, S5 and S6. Transect B is in the middle of the bay and includes two observation sites: S7 and S8. Transect C (not shown in Figure 1A) is at the mouth of Deep Bay, almost parallel to Transect B, and includes five observation sites. The measured data in Transect C were not used for calibration or validation purposes, but as the boundary condition data. According to the water depth, **H** (m), at local measurement time, the velocity measurements were obtained at six vertical levels: 0.0 **H** (surface layer), 0.2 **H**, 0.4 **H**, 0.6 **H**, 0.8 **H** and 1.0 **H** (bottom layer). At each site, current velocities were measured hourly by the ZSX-3 direct-reading flow instrument at each vertical layer. Water samples were collected sequentially from the surface layer to the bottom layer at each site. Five hundred milliliters of each water sample were taken and filtered immediately on a pre-weighted Whatman Cellulose Acetate Membrane filter with a diameter of 47 mm and a nominal pore size of 0.45 micrometers. The filter was stored in a desiccator, which was then combusted in a 500 oven for 3 h and weighed in the laboratory. An analytical balance was used to weigh the filter, with a precision of 0.01 mg. Sediment concentration was determined by the weight difference normalized by the filtered water volume. Salinities were measured by a digital salinity meter from these water samples. It is noted that when the water depth less was than 2 m, no measurements at the surface layer were taken, and measurements were made near the surface layer. In this study, near surface sediment data were used as the surface sediment data when there were no surface sediment measurements. It also should be noted that there was a very small amount of near surface sediment taken at S4 and S6, because the water depths at these two sites were very shallow most of the time, and measurements were taken only near the bottom layer (0.8 **H**).

Figure 1. Model area and *in situ* measurements location (**A**) and the model grids with bathymetry (**B**). FNNR, Futian National Nature Reserve; MPNR, Mai Po Nature Reserve.

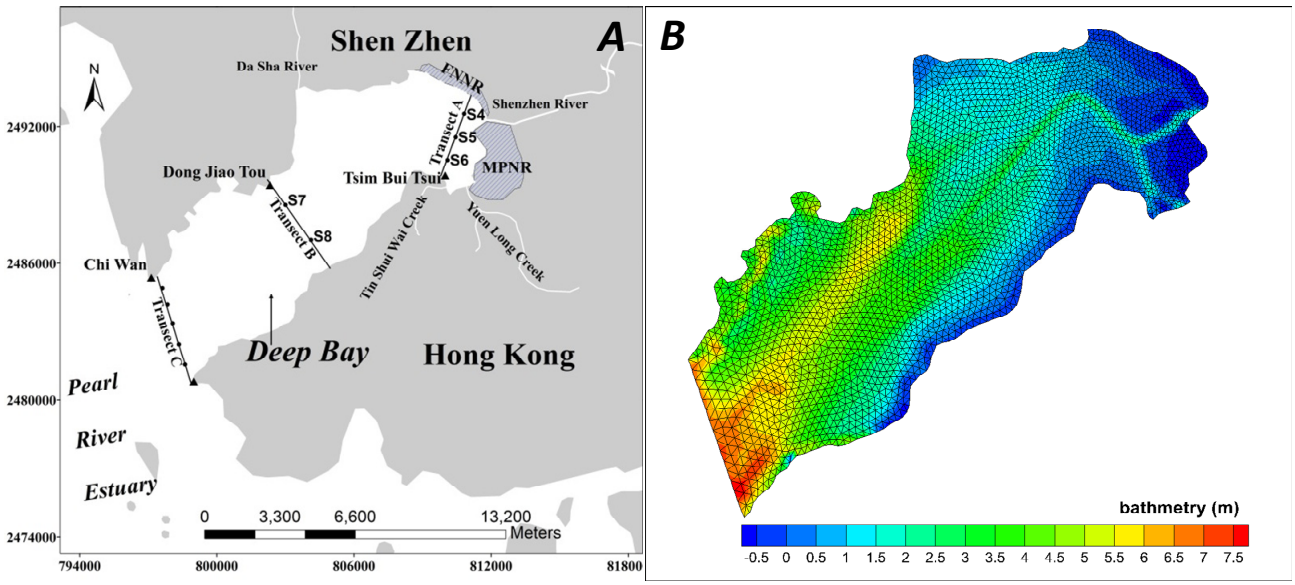

2.2. Model Description and Configuration

The model applied for the calculation of the hydrodynamics and sediment transport in Deep Bay is an unstructured grid, finite volume, free-surface, 3-D primitive equation coastal ocean model

(FVCOM) developed by [18]. Unstructured triangular grids used in FVCOM provide an accurate fit for the geometry of irregular coastlines. A sigma-coordinate transformation was used to represent bottom slope irregularities in the vertical direction. The model simulates water surface elevation, 3D velocity, flooding and drying processes, temperature, salinity, water quality and sediment transport. The FVCOM sediment transport model is based on the Community Sediment Transport Model (CSTM) developed by the U.S. Geological Survey (USGS). It is implemented by solving the three-dimensional advection-dispersion equations. It has been tested on many coastal environment studies for the calculation of current-induced erosion, transport and the deposition of multiple sediment classes and has also been implemented in the well-known Regional Ocean Modeling System (ROMS) [19]. Through analyzing the size distribution of suspended sediment from the field survey data of Deep Bay by Wong and Li [20], it is argued that the median size of suspended sediment in the dry season is 10 μm, and there is no significant difference in the size distribution of suspended sediment in the vertical direction. In this study, cohesive sediment with a dominant median size of the suspended matter was considered to simulate the three-dimensional sediment transport of Deep Bay by FVCOM.

The model grids were generated based on the land boundary with a relatively high resolution (80 m) in the inner bay near the Shenzhen River and a coarser resolution (250 m) at the open boundary. Because the *in situ* measurement was conducted at 0.0 **H**, 0.2 **H**, 0.4 **H**, 0.6 **H**, 0.8 **H** and 1.0 **H** (**H** is water depth), we set six vertical sigma layers in the model in order to facilitate model validation. Hourly wind metrological data at S7 was used as the spatial uniform water surface driving force. The open boundary was driven by tidal elevations measured at Chi Wan and Lan Kok Tsui. Measured sediment concentrations and salinity at the sites of Transect C were also prescribed in the open boundary. Mean flow rates and sediment concentration of Shenzhen, Yuen Long, Tin Shui Wai and Da Sha Rivers (Table 1) in the dry season obtained from the Drainage Services Department of Hong Kong were prescribed in the model. Model run time extended from 0:00, on 10 October, to 24:00, on 20 October in 2004, and the external and internal time steps were 1 s and 10 s. The model was cold started and initialized with zero current velocity. Since the model initial time is in the neap tide period, the sediment concentration and salinity were initialized by horizontally uniform values with the mean observed profiles measured from 11:00, on 17 October, to 15:00, on 18 October. The tidal amplitude was initialized by the *in situ* measured water level on TBT obtained from the Hong Kong Observatory. The model reached a steady state after several tidal cycles of spin-up time until 11:00, on 17 October, when the model calibration and validation were conducted by comparing with *in situ* measurements.

Table 1. The mean flow rates (V) and sediment concentration (C) of four rivers.

Parameter	Shenzhen River	Dasha River	Yuen Long River	Tin Shui Wai River
V (m3/s)	1.4	0.47	0.34	0.23
C (mg/L)	30	10	10	10

3. Methods

3.1. Satellite Sediment Information Retrieval

In this study, we used images from the National Aeronautics and Space Administration (NASA) MODIS data archive website [21]. Two cloud-free MODIS Aqua satellite images were obtained during

the *in situ* measurement period. One is in 13:30, on 17 October, and the other is in 13:30, on 18 October. We selected Level 1 data to correct the atmospheric effect to obtain the water reflectance using the Quick Atmospheric Correction (QUAC) method proposed by Bernstein *et al.* [22]. QUAC is a semi-empirical method that requires no prior information on atmospheric conditions and illumination/viewing geometry at the time of image acquisition, and it is based on several simplistic assumptions. Previous results over turbid waters have shown that QUAC yields accuracies that are comparable to other methods [23], with significantly faster computational speeds and a robust atmospheric correction result.

Using satellite image data to derive sea surface sediment concentration, a relationship between suspended sediment concentration (SSC) and water reflectance must be determined. Such relationships have been proposed through semi-analytical algorithms based on radiative transfer theory [24,25] and, very often, by empirical regression methods. Many empirical regression relationships documented by other researchers have been tested to establish the remote sensing retrieval models of the suspended sediment. These empirical models include linear, exponential, logarithmic statistical relationships, and so forth [8,26,27]. In this study, we tried to establish an empirical regression algorithm for retrieving the sediment concentration from MODIS images.

For MODIS data, traditional bands with a spatial resolution of 1000 m were specifically designed for ocean color observation of open ocean waters. Such bands are not suitable over highly turbid coastal and inland waters for ocean color observation, because the bands saturate and the true signals are unknown [28]. However, a number of investigators have looked to exploit some land/cloud bands that have a spatial resolution of 250 m and 500 m for application to inland and coastal turbid waters [29,30]. These bands contain 645 nm and 555 nm wavelengths, which have been proven to be useful for establishing the sediment retrieval algorithms on the eastern part of Pearl River Estuary in which the Deep Bay is located [31,32]. In this study, the water reflectance on these two bands obtained from MODIS images was used. Because the acquisition time of the used MODIS data is at 13:30, on 17 October and 18 October, the average value of *in situ* measured sediment concentration at 13:00 and 14:00 was used as the measured sediment concentration at 13:30. Based on water reflectance and the *in situ* measured suspended sediment concentration at all sites on Transect A, B and C at the two image acquisition times, the best relationship for representing the model with the square correlation coefficient of 0.835 has been found, and it is shown as follows.

$$SSC = 0.0242\exp[6.3466 \times Rss(645)/Rss(555)\,] \quad (1)$$

where *SSC* denotes the suspended sediment concentration (mg/L) and *Rss*(645) and *Rss*(555) denote the water reflectance on bands 645 nm and 555 nm, respectively. Figure 2 shows the scatter plot of remote sensing reflectance and suspended sediment concentration. The surface sediment concentration was retrieved from the two available images based on this function. The retrieved image reflectance may have unusually high values in the pixels adjacent to the land due to the land reflection effect. This will result in abnormal sediment concentration in the image pixel near the coastline. Therefore, such bad pixels have been deleted manually to ensure a reliable assimilation experiment. Figure 5 shows the retrieved sediment distribution of the two images at 13:30, on 17 October, and 13:30, on 18 October.

Figure 2. Matched *in situ* suspended sediment and remote sensing reflectance retrieved from Moderate Resolution Imaging Spectra-radiometer (MODIS) images.

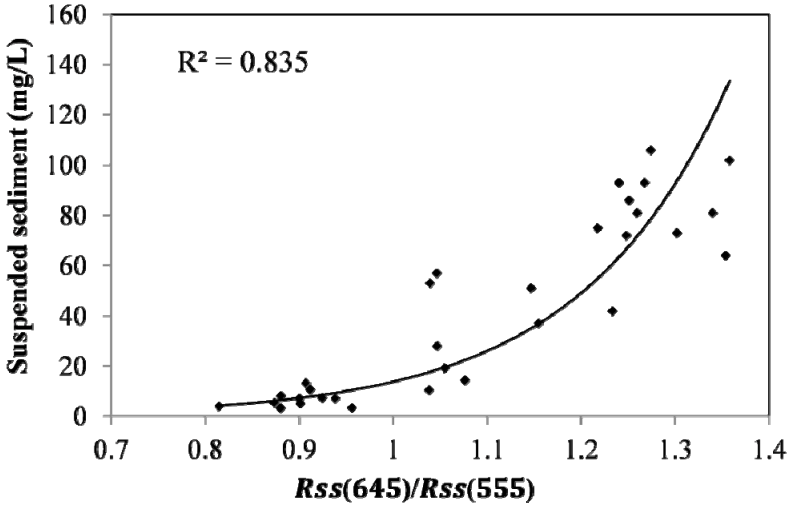

3.2. Assimilation Scheme

In this study, the widely used ocean data assimilation method—the optimal interpolation (OI) algorithm—was employed as the assimilation approach [33,34]. The OI method obtains the statistically optimal state based on model forecasting and observation through least squares estimation. It has the advantage of the simplicity of implementation and its relatively small computation cost, especially for highly nonlinear, high-dimensional ocean model systems. Based on OI, the sediment observations from remote sensing images were interpolated into a model grid using a model forecasted field as a first guess. First, we mapped remote sensing sediment concentration into *n* model grids. The updated sediment concentration field is then obtained from

$$\mathbf{C}ka = \mathbf{C}_k^f + \mathbf{W}_k(\mathbf{C}_k^{rs} - \mathbf{C}_k^f) \quad (2)$$

where **C** is the *n*-dimensional vector of sediment concentration, with superscripts *a*, *f* and *rs* denoting the updated state, the model forecast and remote sensing observation, respectively, and subscript *k* denoting the assimilation time when there is a remote sensing image. The gain, **W**, is an $n \times n$ matrix of weights that determines each observation's influence on the final updated state. Using a principle of minimizing error variance of updated sediment concentration [35], we can argue that $\mathbf{W}_k$ should be:

$$\mathbf{W}_k = \mathbf{P}_k^f(\mathbf{P}_k^f + \mathbf{R}_k)^{-1} \quad (3)$$

where $\mathbf{P}^f$ is the $n \times n$ error covariance matrix of the sediment concentration field from the model forecast and **R** is the $n \times n$ error covariance matrix of the sediment concentration field from remote sensing images. After determining $\mathbf{W}_k$, the updated sediment concentration field is obtained by Equation (2). The model is then integrated to the next forecast time, with the updated field as the initial condition until the next assimilation time.

In order to perform OI, the model forecast error covariance matrix, $\mathbf{P}^f$, and remote sensing error covariance, **R**, in Equation (3) must be determined. In this study, the error variances of model forecast

and remote sensing sediment concentration were obtained through a comparison with *in situ* measured sediment concentration at all sites on three transects. They are computed using the following formula.

$$\sigma_{f,k}^2 = \frac{1}{N}\sum_{i=1}^{N}\left(\mathbf{C}_{i,k}^{f} - \mathbf{C}_{i,k}^{in\ situ}\right)^2 \quad (4)$$

$$\sigma_{rs,k}^2 = \frac{1}{N}\sum_{i=1}^{N}\left(\mathbf{C}_{i,k}^{rs} - \mathbf{C}_{i,k}^{in\ stu}\right)^2 \quad (5)$$

where σ_f^2 , σ_{rs}^2 are the error variances of forecasted sediment concentration and remote sensing sediment concentration, with subscript k denoting the assimilation time. $\mathbf{C}_i^{in\ stu}$ denotes the *in situ* measured sediment concentration at the i-th *in situ* site. N is the number of *in situ* measurement sites. The error variances of model forecast and remote sensing sediment concentration were calculated as 739.84 and 28.09, respectively.

In optimal interpolation, it is often assumed that both model and measurement errors follow a Gaussian distribution, and there is no correlation between measurement error and model error [36]. It is also usually assumed that there is no correlation between measurement errors, so the error covariance matrix, **R**, is a diagonal matrix with an error variance of 28.09 in the diagonal line and 0 in other elements.

For the determination of the model forecast error covariance, $\mathbf{P}^f$, many schemes for calculating forecast error correlations have been proposed and put to practical assimilation application [36,37]. In this study, an exponential correlation model was chosen to define the error correlation. It is assumed that the forecast errors follow a Gaussian distribution, and the error correlation decreases exponentially with the square of the distance [38]. The formulation of the correlation function is given as:

$$\rho = \exp\left[-\frac{(\Delta x)^2+(\Delta y)^2}{R^2}\right] \quad (6)$$

where ρ is the forecast error correlation, Δx, Δy are the distances between two forecast grid points in the x, y directions and R is the correlation length, which limits the influence of interpolated data within a fixed region in optimal interpolation [39]. In this study, the hydrodynamic and sediment transport model first ran "cold" with the provided input data and parameters and was validated by *in situ* measurements. In this study, the hydrodynamic and sediment transport model first ran "cold" with the provided input data and parameters and was validated by *in situ* measurements. Based on the established model, model runs were conducted with two surface sediment concentration images obtained in Section 3.1 sequentially assimilated into the model. In order to achieve a good performance of data assimilation, the optimal forecast error correlation must be determined. By repeatedly assimilating remote sensing sediment using different correlation lengths, an optimal correlation length that produced the best result in the OI was selected. In this study, the root mean square error (RMSE) was calculated for each correlation length at the two assimilation times to evaluate the assimilation performance. The RMSE is calculated as:

$$RMSE = \sqrt{\frac{\sum_{i=1}^{N}(\mathbf{C}_i^a - \mathbf{C}_i^{in\ situ})^2}{N}} \quad (7)$$

where $\mathbf{C}_i^a$ and $\mathbf{C}_i^{in\ situ}$ denote the sediment concentration from OI results and *in situ* measurement sites. N is the number of *in situ* measurements. The RMSE is also used to evaluate the model performance to forecast water level, salinity, current velocity and sediment concentration.

4. Results and Discussion

4.1. Model Calibration and Validation

A well calibrated and validated hydrodynamic and sediment transport model based on FVCOM that simulates the tide and sediment movement of Deep Bay has been built by Zhang *et al.* [40]. However, the model was established for application in the wet season of the bay. For application in the dry season in the present study, all parameters need to be recalibrated. Based on the hydrodynamic and sediment transport model parameters in Zhang *et al.* [40], we use the trial-and-error method to adjust the parameters to achieve a consistent computed result with the measurement. After repeatedly adjustments, an optimal set of parameters has been determined for the model of Deep Bay in the dry season. The final parameters are listed in Table 2.

Table 2. Parameters used in the model of Deep Bay in the dry season.

Parameters	Value
Bottom friction coefficient	0.0024
Sediment median diameter	0.011 mm
Erosion constant	1.2×10^{-5} kg/m^2/s
Critical shear stress for erosion	0.2 N/m^2
Critical shear stress for deposition	0.08 N/m^2
Settling velocity	$W_s = 0.014 \times c^{1.3}$ m/s, $c \geq 60$ mg/L $W_s = 5 \times 10^{-5}$ m/s, $c < 60$ mg/L

Figure 3 shows the comparisons of simulated hydrodynamic and sediment transport model results and corresponding measurements. The comparisons show that the simulated water levels agree well with *in situ* measurements at DJT (Figure 3a) and TBT (Figure 3b). The RMSEs of the computed water level at the two stations are 0.026 m and 0.075 m, respectively. The simulated results from two sites, S5 in Transect A and S7 in Transect B, were selected to compare with the measurements (Figure 3c–j) and for the later analysis. Figure 3c,d demonstrates that the simulated salinities are in good agreement with the measurements at S5 and S7, respectively. The statistics shows that the RMSEs of simulated salinity for all sites are less than 1.8 ppt. By comparing the salinity dynamics at sites S5 and S7 with water level variation at the nearby tidal stations, TBT and DJT, it is found that the salinity transport in the bay is highly correlated with the ebb and flood tidal cycles. The dynamics of salinity show almost the same periodic variation with the tidal levels. This indicates that salinity in the dry season of Deep Bay is largely dominated by brackish water intrusion from the outlet of the bay. However, in the wet season, as shown in Zhang *et al.* [40], the salinity transport in Deep Bay did not show obvious correlation with tidal level variation, but was largely affected by the salinity of the water discharged from rivers.

Figure 3e–h demonstrates that the simulated depth-averaged current velocity and direction are reasonably consistent with corresponding measurements at sites S5 (Figure 3e,g) and S7 (Figure 3f,h). The RMSEs of simulated current velocity and direction for all measurement sites are less than 0.118 ms^{-1} and 19.7°, respectively. Figure 3i,j shows a comparison of simulated depth-averaged sediment concentration with measurements at S5 and S7, respectively. It shows that, due to the complex

sediment dynamics, the sediment is not precisely forecasted, especially when the sediment concentration is relatively low. The time series of simulated sediment demonstrated an apparent smooth dynamic trend compared to *in situ* measurements, which exhibit a more irregular cycle. However, both the measured and simulated sediment concentrations exhibit a dynamic trend that is similar to the complicated dynamics of current velocities. This finding indicates that sediment transport is dominated by the current dynamics of the bay, which is in line with the previous study of Zhang *et al.* [40]. Because deposited sediments need time to be resuspended to the water column after the occurrence of the maximum ebbing or flooding tidal period, the maximum value of sediment concentration lags behind the maximum value of current velocity by about one hour.

Figure 3. Validation of model results. (**a**) the water level at Tsim Bui Tsui (TBT); (**b**) water level Dong Jiao Tou (DJT); (**c**) the depth-averaged salinity at S5; (**d**) the depth-averaged salinity at S7; (**e**) the depth-averaged current velocity at S5; (**f**) the depth-averaged current velocity at S7; (**g**) the current direction at S5; (**h**) the current direction at S7; (**i**) the sediment concentration at S5; (**j**) the sediment concentration at S7.

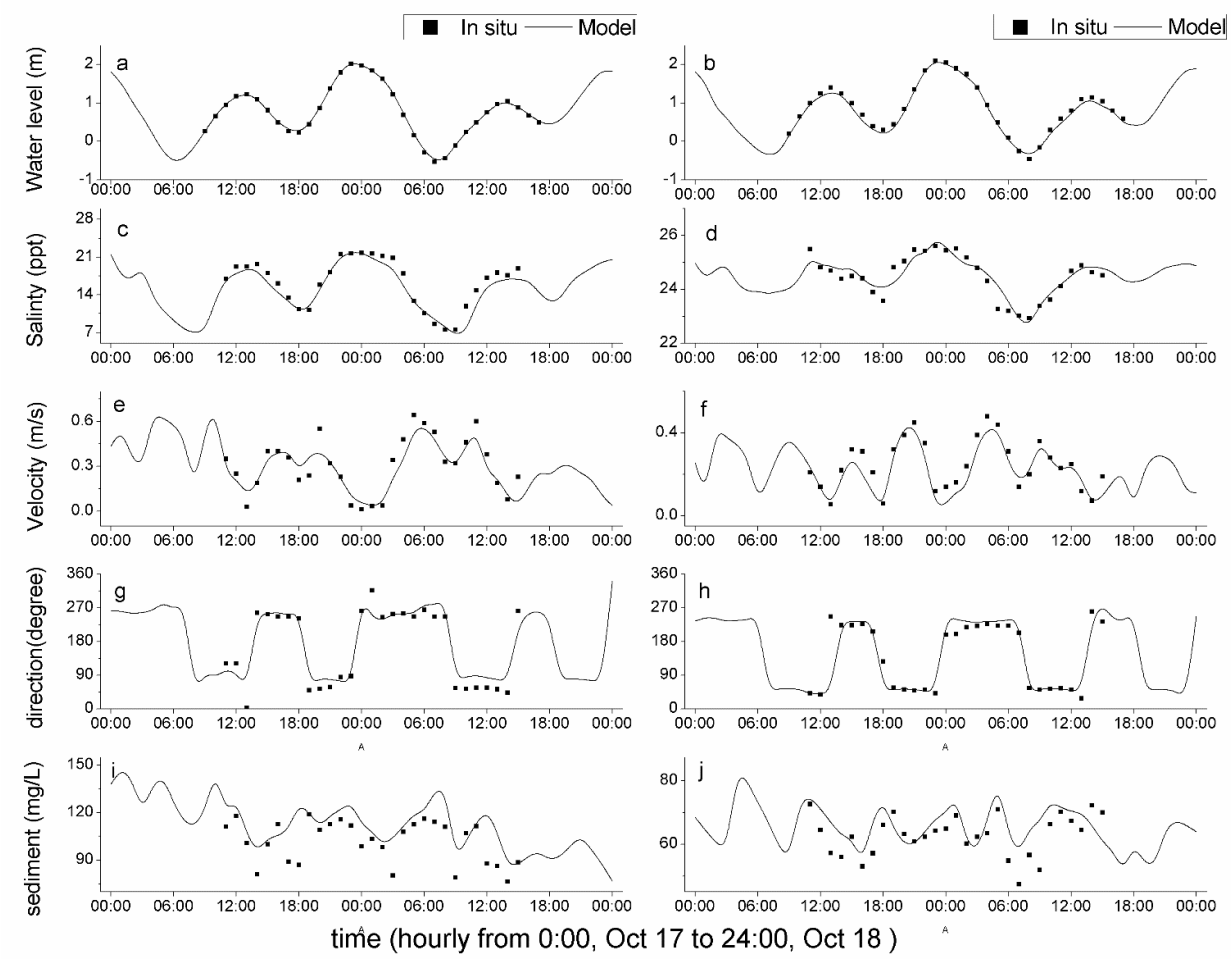

Figure 4 compares the profiles of measured and modeled current velocity, sediment concentration and salinity at the maximum flood (11:00, on 17 October) and the maximum ebb (4:00, on 18 October) periods. The comparisons show that the simulated results can reasonably represent the profiles denoted by the measurements. It can be seen that the vertical velocities at the maximum ebb period are

relatively higher than the ones at the maximum flood period, but the vertical sediment concentrations are higher at the maximum flood period. This is probably because tidal transport dominates the sediment dynamic at the maximum flood period, when a large amount of sediments are carried into the bay from the outer bay. It should be noted that, at the maximum ebb period, the high concentrations occurred at the near-bottom layers, which may be caused by the bottom resuspension, because the tidal flow reached the maximum current velocity. The vertical profiles of salinity demonstrate unobvious vertical stratification. It can be seen that the salinities shown in the profile at the maximum flood period are relatively higher than those at the maximum ebb period. This is because the tidal level at the maximum flood period (0.95 m) is higher than that at the maximum ebb period (0.64 m), so more salt water is brought into the bay at the maximum flood period.

Figure 4. Vertical profile validation of model results at S7. (**A**) the current velocity at the maximum flood period at 11:00, on 17 October (**a**,**b**) and the maximum ebb period at 4:00, on 18 October (**c**,**d**); (**B**) the sediment concentration at the maximum flood period at 11:00, on 17 October (**a**,**b**) and the maximum ebb period at 4:00, on 18 October (**c**,**d**); (**C**) the salinity at the maximum flood period at 11:00, on 17 October (**a**,**b**) and the maximum ebb period at 4:00, on 18 October (**c**,**d**). Notes: **a**, **c** representing the measured profiles and **b**, **d** representing the simulated profiles.

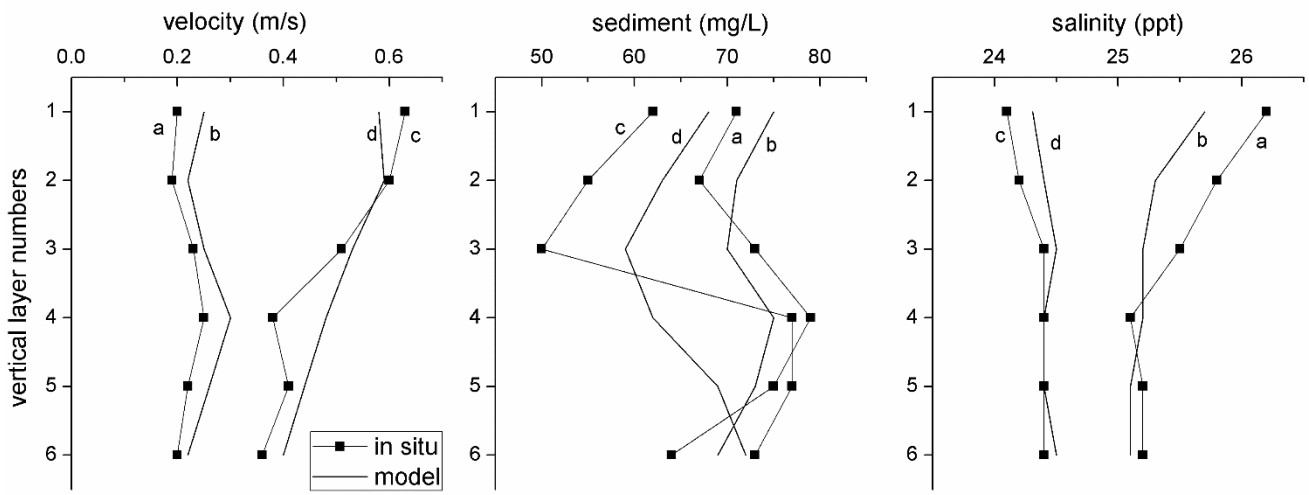

4.2. Assimilation Result Analysis

4.2.1. Sediment Correction at the Data Assimilation Time

In order to choose an optimal forecast error correlation length, a series of data assimilation experiments were repeatedly conducted by changing the correlation length, trying 250, 500, 750, …, 2500 m. It is found that when the correlation length is 1500 m, a minimum *RMSE* of 13.8mg/L was obtained by comparing with *in situ* measurements at the assimilation time. Therefore, we use 1500 m as the correlation length in the assimilation.

Figure 5 shows the comparison of sediment concentration from *in situ*, model and OI results at the two assimilation times. It shows that the model overestimated the surface sediment concentration at

most of the sites, and they are clearly improved by OI. The improvement is also pronounced for the underestimated sediment concentration at sites S4, S6 and S8 at the second assimilation time. For all validation sites, the relative errors of the model vary from 4.3% to 68.1%, and for OI, results vary from 0.8% to 31.9%. The OI results reduce the errors by 36%–91%.

Optimal interpolation is expected to improve the prediction of the spatial distribution of the sediment concentration by correcting the model results with remote sensing data by capturing their error information. Figure 6 shows the spatial distribution of sediment concentration from model, remote sensing images and OI results at the two assimilation times. It is observed that the OI results display a better spatial consistency with remote sensing sediment distribution. More detailed surface sediment distributions are captured in the OI results, and it is particularly evident in the shallow inner region of Deep Bay. The comparisons reveal that both the information from the model results and the remote sensing sediment concentration is retained in the OI results. This is obvious in coastal areas, where the sediment concentration is filled up by interpolating remote sensing sediment and model results. Table 3 displays the statistical characteristics of sediment concentration difference between OI and model results and between OI and remote sensing results. It can be seen that the mean value and variance of difference between OI and remote sensing results are smaller than those between OI and model results. This indicates that more information in the OI results comes from the remote sensing image. This is possibly because the remote sensing sediment concentration is more accurate than the model results.

Figure 5. Surface sediment concentration from *in situ*, model and optimal interpolation (OI) results at all sites at the first assimilation time (13:30, on 17 October) and the second assimilation time (13:30, on 18 October). Note that because the *in situ* measurements were collected hourly and there are no *in situ* sediment measurements during the satellite image acquisition time, therefore *in situ* measurements at the assimilation time used in this figure are the average values of the *in situ* sediment concentration of a half an hour before and a half an hour after the assimilation time.

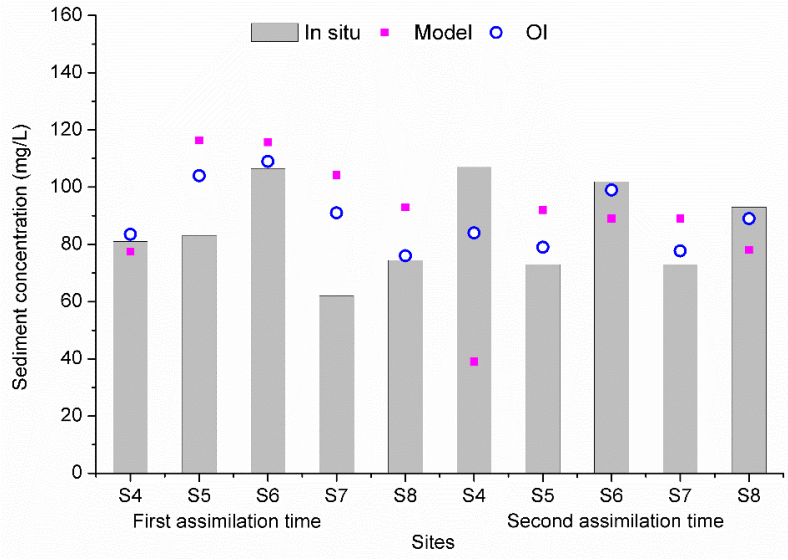

Figure 6. Comparison of the sediment spatial distribution from those retrieved from (**A**) model results (Model); (**B**) remote sensing images (RS); and (**C**) OI results at the first assimilation time (13:30, on 17 October) and from (**D**) model results (Model); (**E**) remote sensing images (RS); and (**F**) OI results at the second assimilation time (13:30, on 18 October).

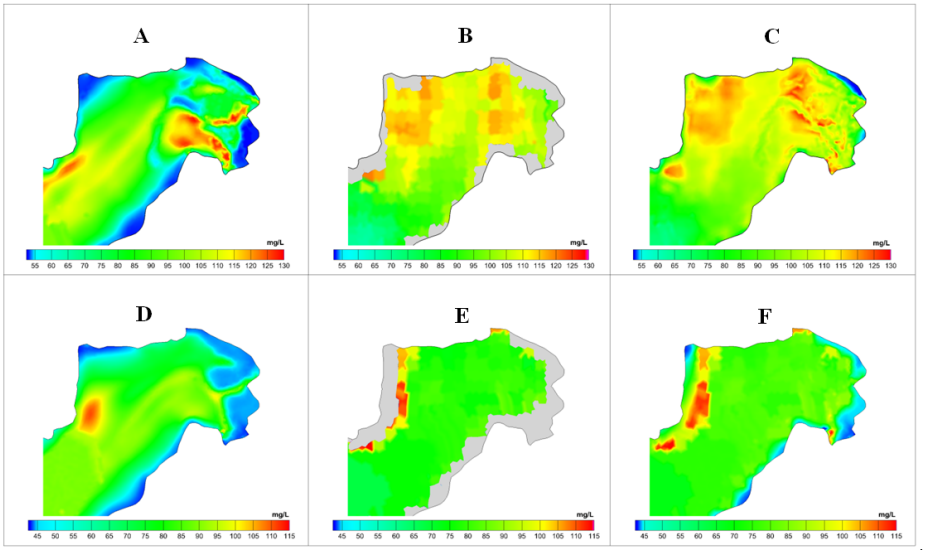

Table 3. The mean value and variance of the spatial difference between OI results and model results and the spatial difference between OI results and remote sensing sediment at the two assimilation times.

Assimilation time	Difference	Mean (mg/L)	Variance (mg/L)
AT1	OI-RS	2.5	21.16
	OI-Model	7.8	492.84
AT2	OI-RS	1.4	8.41
	OI-Model	−10.6	979.69

4.2.2. Temporal Effect of Data Assimilation

Figure 7 shows the time series of the surface sediment concentration of *in situ* measurements, model results with and without data assimilation, together with the remote sensing sediment at the assimilation time at sites S5, S7 and S8. The figure shows that the effect of remote sensing sediment assimilation on the model result was limited, because the remote sensing image was only a snap shot of the surface sediment concentration at a short period of time. It is found that, after assimilating the first sediment image into the model, the temporal effect lasts about four and half hours, until the water level reached its lowest; while the temporal effect of assimilating the second sediment image lasts about two hours, until the water level reaches its highest. This suggests that the temporal effect ends at the time when tidal currents alternate their flow directions. At the same time, the direction of horizontal sediment transport also tends to change. Thus, the disappearance of the temporal effect brought by remote sensing data assimilation may be owed to the rapid dynamic behavior of sediment transport in a tidal cycle of the bay. However, more powerful data assimilation schemes, like the four-dimensional variational method, which can handle observations that are distributed within a

time interval, can be used to achieve a global optimization or correction of the whole model forecasted state.

Figure 7. The time series of *in situ* measured surface sediment (half hourly) and forecasted sediment from the model with and without assimilation (half hourly) at sites S5 (**A**); S7 (**B**); and S8 (**C**). The remote sensing sediment at the assimilation time is also shown.

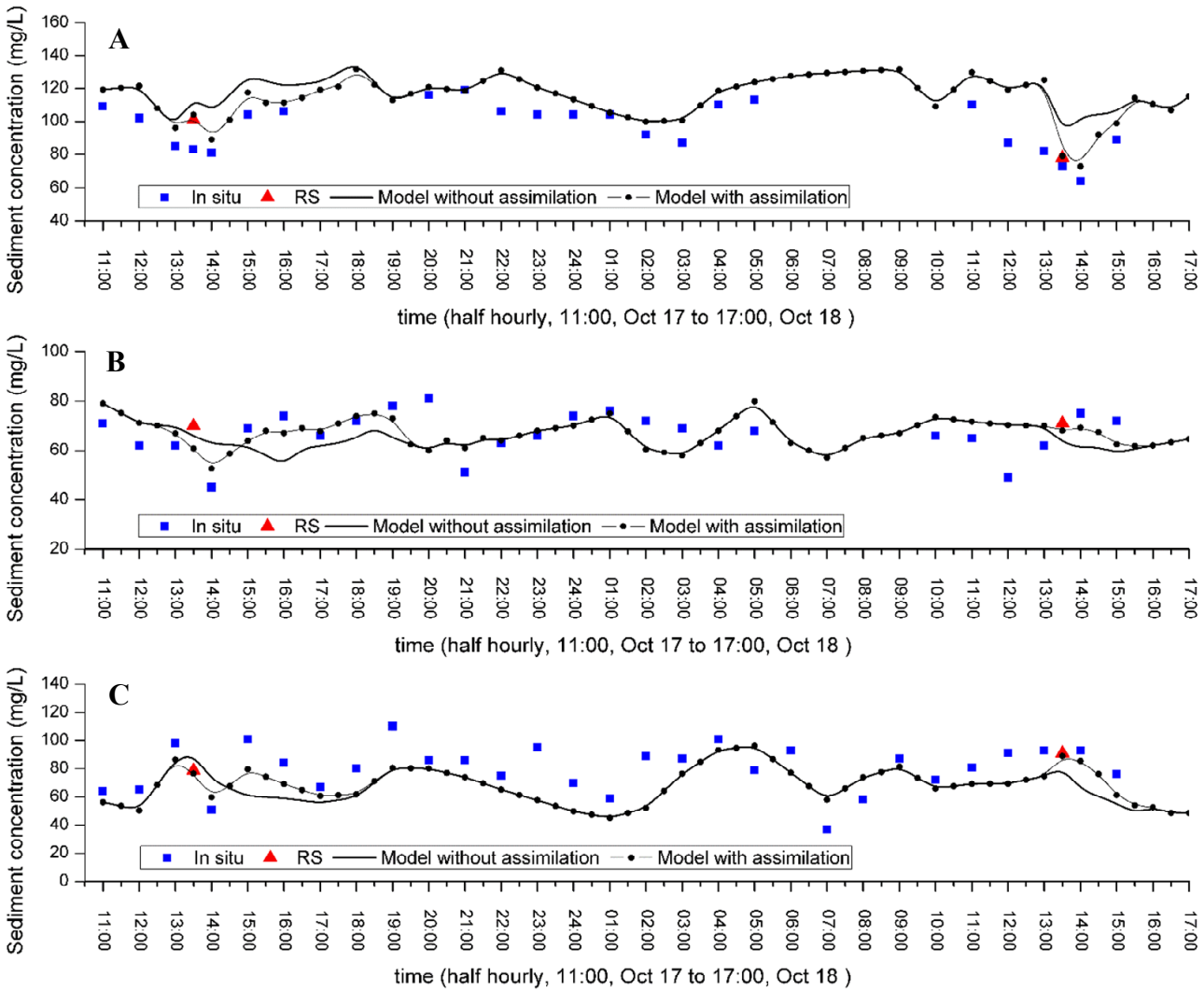

Despite the limited temporal effect on the model forecast brought by remote sensing data assimilation, the results have been improved to a large extent at the affected time. It could be seen in Figure 7 that the model with data assimilation improved the forecasts results, to agree better with the *in situ* measurements. In particular, it can be apparently observed at S7 and S8 after the first assimilation time (between 14 h and 18 h) that the model forecast with data assimilation caught the oscillation of sediment concentration, which was not seen from the model results without data assimilation. It is observed that, although the assimilated remote sensing sediment showed greater deviation from *in situ* measurement at S7 at the first assimilation time, the improving of assimilation results is still obvious. This reveals the validity of data assimilation for providing a more accurate state by catching the errors from remote sensing data and model results. Table 4 tabulated the RMSE statistics of the simulated surface sediment concentration from the model with and without remote

sensing data assimilation at S5, S7 and S8. It shows that the model with data assimilation reduces the *RMSE* of the forecasted surface sediment concentration by at least 47.8% over the model without data assimilation. In short, the data assimilation scheme shows the validity of improving model forecasting on the whole.

Table 4. Statistics of *RMSE* (mg/L) over surface sediment concentration and the depth-averaged sediment concentration from the model results with and without assimilation in the limited effect time (four and a half hours after the first assimilation time and one and a half hours after the second assimilation time, along with the relative *RMSE* reduction) [a]. Note that the *RMSE*s of the simulated surface sediment at S4 and S6 were not calculated, because no *in situ* surface sediment concentration was taken at the two sites.

Sites	Model without OI	Model with OI	Relative *RMSE* Reduction
surface sediment			
S5	18.2	7.5	58.8%
S7	13	6.1	53.1%
S8	25.1	13.1	47.8%
depth-averaged sediment			
S4	17.5	11.2	36.0%
S5	25.2	9.3	63.0%
S6	29.4	15.4	47.6%
S7	15.5	9.7	37.4%
S8	21.7	11.9	45.2%

Note: [a] relative *RMSE* reduction = (*RMSE*_Model-*RMSE*_OI)/*RMSE*_Model.

The temporal ability produced by assimilating the surface sediment concentration is not limited to the upper surface layer. As an integral part of the sediment distribution in the water column, the surface sediment is involved in sediment settling and vertical mixing in the sediment transport model. Therefore, updating the surface sediment concentration by assimilation has the potential to change the sediment movement trend, hence affecting all of the simulated sediment vertical profiles. In this study, such a temporal ability in the vertical column has been observed. However, the temporal effect of data assimilation still did not remain too long in the water column and, at most, lasted for one hour. In consideration of the small effect caused by a very small amount of discharged sediment from the rivers (see Table 1), this may be owed to the rapid sediment exchange between the sea bed and the water column. However, from the *RMSE* statistics of simulated depth-averaged sediment concentration in the limit effect time, it can be seen that the model with data assimilation reduced the *RMSE* of the simulated depth-averaged sediment concentration by 36% against the model without data assimilation. This reveals the potential ability of surface sediment data assimilation to improve three-dimensional sediment concentration forecasting. Figure 8 demonstrates the comparison of the vertical sediment profile from measurements, the model with and that without data assimilation at S7 half an hour after the first assimilation time and the second assimilation time. A positive change of sediment distribution from the model with data assimilation can be seen in the figure. Effective schemes on how to improve the sediment modeling in the lower layer within a longer forecast time by assimilating surface sediment should be further explored.

Figure 8. Vertical distribution comparison at site S7 at half an hour after the first assimilation time (**A**) and at half an hour after the second assimilation time (**B**).

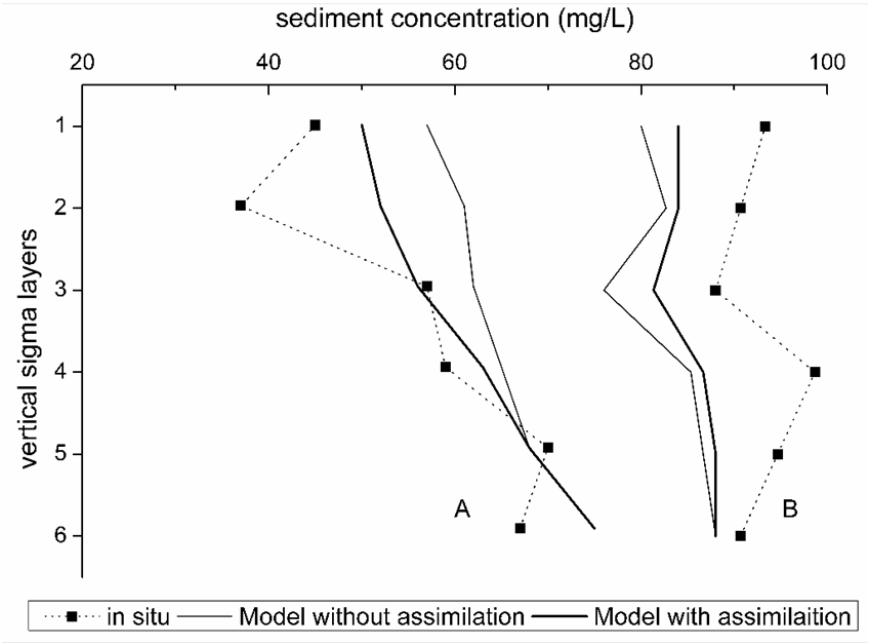

5. Conclusions and Outlook

The present study explored the integration of remote sensing data with a three-dimensional sediment transport model to improve model prediction. Two scenes of surface sediment data derived from MODIS satellite images were sequentially assimilated into the sediment transport model of Deep Bay in a tidal cycle. The results showed that the data assimilation can improve the sediment transport modeling. The model with remote sensing sediment data assimilation produced more accurate sediment dynamics than the model without data assimilation. The temporal ability of the data assimilation on both the surface transport and the vertical mixing were observed. Due to the rapid sediment transport and resuspension induced by the current flows in this tidally-dominated bay, the temporal ability of data assimilation was limited to a maximum of four and a half hours. In a future study, multi-platform remote sensing data could be employed to narrow the gap of assimilation time to achieve a long-term effect on the model forecast and prediction. Further work can also explore assimilation schemes to improve the sediment prediction of the entire vertical water column by assimilating the surface sediment concentration. The error correlation of the computed sediment concentration between the surface layer and the lower column can be considered in the improved schemes. Other sophisticated assimilation methods, like the ensemble Kalman filter and the variational scheme, could also be alternatives. To conclude, this work provides an insight into improving sediment transport prediction in highly dynamic coastal zones using remote sensing data assimilation. The present method can be applied to other coastal and inland water areas of interest for monitoring and modeling of the suspended sediment concentration, as well as other ocean color parameters, such as chlorophyll. Moreover, the combination of assimilating both remote sensing sediment concentration and field measured current velocity into a three-dimensional model may also be a promising idea. Because current dynamics largely govern the sediment movements in coastal waters, it is likely

that the improved current circulation will result in a better prediction of the suspended sediment concentration.

Acknowledgments

This work was supported by the Hong Kong Research Grants Council (grant no. B-Q23G), the National Natural Science Foundation of China (grant No. 41331174, 41101415), the 863 project (grant No. 2012AA12A304) and the Program for Changjiang Scholars and Innovative Research Teams in University (IRT1278). We thank Professor Changsheng Chen at SMAST/UMASSD for providing the source code of FVCOM and the Drainage Services Department of the Hong Kong for providing the measurement data. We also would like to express our thanks to the anonymous reviewers for constructive comments that helped to improve the quality of this manuscript.

Conflicts of Interest

The authors declare no conflict of interest.

References

1. Onishi, Y.; Serne, J.; Arnold, E.; Cowan, C.; Thompson, F. *Critical Review: Radionuclide Transport, Sediment Transport, Water Quality, Mathematical Modelling and Radionuclide Adsorption/desorption Mechanism*; NUREG/CR-1322; Pacific Northwest Laboratory: Richland, DC, USA, 1981; p.512.
2. Smith, P.J.; Dance, S.L.; Nichols, N.K. A hybrid data assimilation scheme for model parameter estimation: Application to morphodynamic modelling. *Comput. Fluids* **2011**, *46*, 436–441.
3. Amoudry, L.O.; Souza, A.J. Deterministic coastal morphological and sediment transport modeling: A review and discussion. *Rev. Geophys.* **2011**, *49*, doi:10.1029/2010RG000341.
4. Stroud, J.R.; Lesht, B.M.; Schwab, D.J.; Beletsky, D.; Stein, M.L. Assimilation of satellite images into a sediment transport model of Lake Michigan. *Water Resour. Res.* **2009**, *45*, doi:10.1029/2007WR006747.
5. El Serafy, G.Y.H.; Mynett, A.E. Improving the operational forecasting system of the stratified flow in Osaka Bay using an ensemble Kalman filter-based steady state Kalman filter. *Water Resour. Res.* **2008**, *44*, W06416.
6. Gregg, W. Assimilation of SeaWiFS ocean chlorophyll data into a three-dimensional global ocean model. *J. Mar. Syst.* **2008**, *69*, 205–225.
7. Pleskachevsky, A.; Gayer, G.; Horstmann, J.; Rosenthal, W. Synergy of satellite remote sensing and numerical modeling for monitoring of suspended particulate matter. *Ocean Dyn.* **2005**, *55*, 2–9.
8. Miller, R.L.; McKee, B.A. Using MODIS Terra 250 m imagery to map concentrations of total suspended matter in coastal waters. *Remote Sens. Environ.* **2004**, *93*, 259–266.
9. Kouts, T.; Sipelgas, L.; Savinits, N.; Raudsepp, U. Environmental monitoring of water quality in coastal sea area using remote sensing and modeling. *Environ. Res. Eng. Manag.* **2007**, *1*, 6.

10. Chen, X.; Lu, J.; Cui, T.; Jiang, W.; Tian, L.; Chen, L.; Zhao, W. Coupling remote sensing retrieval with numerical simulation for SPM study—Taking Bohai Sea in China as a case. *Int. J. Appl. Earth Obs. Geoinf.* **2010**, *12*, S203–S211.
11. Yang, Z. Variational inverse parameter estimation in a cohesive sediment transport model: An adjoint approach. *J. Geophys. Res.* **2003**, *108*, doi:10.1029/2002JC001423.
12. Margvelashvili, N.; Andrewartha, J.; Herzfeld, M.; Robson, B.J.; Brando, V.E. Satellite data assimilation and estimation of a 3D coastal sediment transport model using error-subspace emulators. *Environ. Model. Softw.* **2013**, *40*, 191–201.
13. EI Serafy, G.Y.; Eleveld, M.A.; Blaas, M.; Kessel, T.; Aguilar, S.G.; Woerd, H.J. Improving the description of the suspended particulate matter concentrations in the southern North Sea through assimilating remotely sensed data. *Ocean Sci. J.* **2011**, *46*, 179–204.
14. Lau, S.S.S.; Chu, L. The significance of sediment contamination in a coastal wetland, Hong Kong, China. *Water Res.* **2000**, *34*, 379–386.
15. Qin, H.P.; Ni, J.R.; Borthwick, A.G.L. Harmonized optimal postreclamation coastline for Deep Bay, China. *J. Environ. Eng.* **2002**, *128*, 10.
16. Wang, Y.; Gu, J. Influence of temperature, salinity and pH on the growth of environmental Aeromonas and Vibrio species isolated from Mai Po and the Inner Deep Bay Nature Reserve Ramsar Site of Hong Kong. *J. Basic Microbiol.* **2005**, *45*, 83–93.
17. Zhang, J.; Cai, L.; Yuan, D.; Chen, M. Distribution and sources of polynuclear aromatic hydrocarbons in Mangrove surficial sediments of Deep Bay, China. *Mar. Pollut. Bull.* **2004**, *49*, 479–486.
18. Chen, C.; Huang, H.; Beardsley, R.C.; Liu, H.; Xu, Q.; Cowles, G. A finite volume numerical approach for coastal ocean circulation studies: Comparisons with finite difference models. *J. Geophys. Res.* **2007**, *112*, doi:10.1029/2006JC003485.
19. Chen, C.; Liu, H.; Beardsley, R.C. An unstructured grid, finite-volume, three-dimensional, primitive equations ocean model: application to coastal ocean and estuaries. *J. Atmos. Ocean. Technol.* **2003**, *20*, 159–186.
20. Wong, S.H.; Li, Y.S. Hydrographic surveys and sedimentation in Deep Bay, Hong Kong. *Environ. Geol. Water Sci.* **1990**, *15*, 111–118.
21. MODIS Web. Available online: http://modis.gsfc.nasa.gov/ (accessed on 18 September 2013).
22. Bernstein, L.S.; Adler-Golden, S.M.; Sundberg, R.L.; Levine, R.Y.; Perkins, T.C.; Berk, A.; Ratkowski, A.J.; Felde, G.; Hoke, M.L. A New Method for Atmospheric Correction and Aerosol Optical Property Retrieval for VIS-SWIR Multi- and Hyperspectral Imaging Sensors: QUAC (QUick Atmospheric Correction). In Proceedings of Geoscience and Remote Sensing Symposium, 2005, Seoul, Korea, 25–29 July 2005; pp. 3549–3552.
23. Moses, W.J.; Gitelson, A.A.; Perk, R.L.; Gurlin, D.; Rundquist, D.C.; Leavitt, B.C.; Barrow, T.M.; Brakhage, P. Estimation of chlorophyll-a concentration in turbid productive waters using airborne hyperspectral data. *Water Res.* **2012**, *46*, 993–1004.
24. Dekker, A.G.; Vos, R.J.; Peters, S.W.M. Analytical algorithms for lake water TSM estimation for retrospective analyses of TM and SPOT sensor data. *Int. J. Remote Sens.* **2002**, *23*, 15–35.
25. Volpe, V.; Silvestri, S.; Marani, M. Remote sensing retrieval of suspended sediment concentration in shallow waters. *Remote Sens. Environ.* **2011**, *115*, 44–54.

26. Doxaran, D.; Froidfond, J-M.; Lavender, S.; Castaing, P. Spectral signature of highly turbid waters application with SPOT data to quantify suspended particulate matter concentrations. *Remote Sens. Environ.* **2002**, *81*, 149–161.
27. Han, Z.; Jin, Y.Q.; Yun, C.X. Suspended sediment concentrations in the Yangtze River estuary retrieved from the CMODIS data. *Int. J. Remote Sens.* **2006**, *27*, 4329–4336.
28. Feng, L.; Hu, C.; Chen, X.; Song, Q. Influence of the Three Gorges Dam on total suspended matters in the Yangtze Estuary and its adjacent coastal waters: Observations from MODIS. *Remote Sens. Environ.* **2014**, *140*, 779–788.
29. Hu, C.; Chen, Z.; Clayton, T.D.; Swarzenski, P.; Brock, J.C.; Muller-Karger, F.E. Assessment of estuarine water-quality indicators using MODIS medium-resolution bands: Initial results from Tampa Bay, FL. *Remote Sens. Environ.* **2004**, *93*, 423–441.
30. Wang, L.; Zhao, D.; Yang, J.; Chen, Y. Retrieval of total suspended matter from MODIS 250 m imagery in the Bohai Sea of China. *J. Oceanogr.* **2012**, *68*, 719–725.
31. Xi, H.; Zhang, Y. Total suspended matter observation in the Pearl River estuary from *in situ* and MERIS data. *Environ. Monit. Assess.* **2010**, *177*, 563–574.
32. Liu, D.; Fu, D.; Xu, B.; Shen, C. Estimation of total suspended matter in the Zhujiang (Pearl) River estuary from Hyperion imagery. *Chin. J. Oceanol. Limnol.* **2012**, *30*, 16–21.
33. Carton, J.A.; Chepurin, G.; Cao, X. A simple ocean data assimilation analysis of the global upper ocean 1950–95. Part I: Methodology. *J. Phys. Oceanogr.* **2000**, *30*, 294–309.
34. Fox, D.N.; Eague, W.J.T.; Barron, A.N. The modular ocean data assimilation system (MODAS). *J. Atmos. Ocean. Technol.* **2002**, *19*, 240–252.
35. Daley, R. *Atmospheric Data Analysis*; Cambridge University Press: Cambridge, UK, 1991; Volume 2.
36. Larsen, J.; Høyer, J.L.; She, J. Validation of a hybrid optimal interpolation and Kalman filter scheme for sea surface temperature assimilation. *J. Mar. Syst.* **2007**, *65*, 122–133.
37. Høyer, J.L.; She, J. Optimal interpolation of sea surface temperature for the North Sea and Baltic Sea. *J. Mar. Syst.* **2007**, *65*, 176–189.
38. Mangiarotti, S.; Martinez, J.M.; Bonnet, M.P.; Buarque, D.C.; Filizola, N.; Mazzega, P. Discharge and suspended sediment flux estimated along the mainstream of the Amazon and the Madeira Rivers (from *in situ* and MODIS Satellite Data). *Int. J. Appl. Earth Obs. Geoinf.* **2013**, *21*, 341–355.
39. Xie, J.; Zhu, J. Ensemble optimal interpolation schemes for assimilating Argo profiles into a hybrid coordinate ocean model. *Ocean Model.* **2010**, *33*, 283–298.
40. Zhang, P.; Wai, O.W.H.; Chen, X.; Lu, J. Modeling sediment transport with current velocity assimilation in Deep Bay, Hong Kong, China. In Proceedings of 35th IAHR World Congress, Chengdu, China, 8–13 September 2013; p. 1–6.